First Application of 3D Peripheral Plasma Transport Code EMC3-EIRENE to Heliotron J*)

Ryota MATOIKE, Gakushi KAWAMURA[2,3], Shinsuke OHSHIMA[1], Masahiro KOBAYASHI[2,3],
Yasuhiro SUZUKI[2,3], Kazunobu NAGASAKI[1], Suguru MASUZAKI[2], Shinji KOBAYASHI[1],
Satoshi YAMAMOTO[1], Shinichiro KADO[1], Takashi MINAMI[1], Hiroyuki OKADA[1],
Shigeru KONOSHIMA[1], Toru MIZUUCHI[1], Hirohiko TANAKA[4], Hiroto MATSUURA[5],
Yuhe FENG[6] and Heinke FRERICHS[7]

Graduate School of Energy Science, Kyoto University, Gokasyo, Uji 611-0011, Japan
[1] *Institute of Advanced Energy, Kyoto University, Uji 611-0011, Japan*
[2] *National Institute for Fusion Science, National Institutes of Natural Sciences, Toki 509-5292, Japan*
[3] *Department of Fusion Science, Graduate University for Advanced Studies, Toki 509-5292, Japan*
[4] *Graduate School of Engineering, Nagoya University, Nagoya 464-8603, Japan*
[5] *Graduate School of Engineering, Osaka Prefecture University, Osaka 599-8531, Japan*
[6] *Max-Planck Institute for Plasma Physics, Greifswald, Germany*
[7] *University of Wisconsin-Madison, Wisconsin, U.S.A.*

(Received 9 January 2019 / Accepted 5 April 2019)

The 3D peripheral plasma and neutral transport code, EMC3-EIRENE was applied to the Heliotron J with a wide and flexible controllability of magnetic configuration. This code requires a three-dimensional (3D) grid with high resolution in the peripheral plasma region to reproduce the fine plasma structure. The grid generation tool, FLARE, was utilized to create the grid in conjunction with the code developed to arbitrarily set the outer boundary of the peripheral grid. After setting up the 3D grid, we carried out the EMC3-EIRENE calculation successfully for the first time in the Heliotron J's standard configuration. In addition, the convergence of the iterative calculation and the effects of different grid resolutions upon the calculation were investigated. A good numerical convergence was obtained, and the influence of resolution was observed in the electron density in the divertor region.

Keywords: EMC3-EIRENE, Scrape-Off Layer, divertor, transport, modeling, Heliotron J

DOI: 10.1585/pfr.14.3403127

1. Introduction

Design of divertor is an essentially important issue to control extremely high heat and particle fluxes in the divertor of fusion reactors [1]. For instance, at ITER, the heat load is estimated to be 10 MWm^{-2} under steady-state discharge [2]. Many efforts have been dedicated to reducing heat and particle fluxes to the divertor [3,4], and magnetic field topology is one of the keys for controlling the heat load to the surfaces. The heat and particle deposition profiles depend strongly upon the connection length distributions of the magnetic field on the divertor plates [5]. Helical devices inherently have a three-dimensional (3D) magnetic field configuration, and the divertor has a 3D structure as well. The 3D effects of the peripheral magnetic field are also discussed in tokamak devices by introducing resonant magnetic perturbation coils to control the edge localized modes [6,7]. Therefore, analysis of the 3D effect of magnetic field structure and modeling of peripheral plasma transport is needed. The peripheral transport code, EMC3-EIRENE [8, 9], has been used to model scrape-off layer (SOL) -divertor plasmas and plasma-surface interactions on stellarators including W7-X [10–12] and LHD [13–17], and has also been applied to tokamak devices [18, 19]. Heliotron J [20] is a helical-axis heliotron device with a high controllability of configuration. The dependence of electron temperature, density and heat/particle flux upon the magnetic configuration of divertor plasmas has been discussed using the divertor probe array (DPA) [21–23]; however, no comparison between experiment and simulation of SOL plasma has yet been performed. In this study, we apply the EMC3-EIRENE code to Heliotron J for 3D modeling of peripheral plasma for the first time. The grid generation procedure, typical calculation results, and dependence of calculation results upon different spatial grid resolutions are discussed.

---

author's e-mail: matoike.ryota.62c@st.kyoto-u.ac.jp

*) This article is based on the presentation at the 27th International Toki Conference (ITC27) & the 13th Asia Pacific Plasma Theory Conference (APPTC2018).

2. Numerical Modeling of Heliotron J SOL Plasma

2.1 EMC3-EIRENE code

The peripheral transport code EMC3-EIRENE is used to model the Heliotron J plasma. This code solves the Braginskii's fluid equations below using a Monte Carlo (MC) method in a 3D grid with a field-aligned structure. The conservation of mass, conservation of momentum, conservation of energy for electrons and ions respectively read

$$\nabla_{\parallel}\cdot(n\mathbf{v}_{\parallel}) + \nabla_{\perp}\cdot(-D\nabla_{\perp}n) = S_{\mathrm{p}}, \tag{1}$$

$$\begin{aligned}&\nabla_{\parallel}\cdot(m_{\mathrm{i}}n\mathbf{v}_{\parallel}\mathbf{v}_{\parallel} - \eta_{\parallel}\nabla_{\parallel}\mathbf{v}_{\parallel})\\ &\quad +\nabla_{\perp}\cdot(-m_{\mathrm{i}}\mathbf{v}_{\parallel}D\nabla_{\perp}n - \eta_{\perp}\nabla_{\perp}\mathbf{v}_{\parallel}) = \nabla_{\parallel}p + S_{\mathrm{m}},\end{aligned} \tag{2}$$

$$\begin{aligned}&\nabla_{\parallel}\cdot\left(-\kappa_{\mathrm{e}}\nabla_{\parallel}T_{\mathrm{e}} + \frac{5}{2}nT_{\mathrm{e}}\mathbf{v}_{\parallel}\right)\\ &\quad +\nabla_{\perp}\cdot\left(-\chi_{\mathrm{e}}n\nabla_{\perp}T_{\mathrm{e}} - \frac{5}{2}T_{\mathrm{e}}D\nabla_{\perp}n\right)\\ &= -k(T_{\mathrm{e}} - T_{\mathrm{i}}) + S_{\mathrm{ee}},\end{aligned} \tag{3}$$

$$\begin{aligned}&\nabla_{\parallel}\cdot\left(-\kappa_{\mathrm{i}}\nabla_{\parallel}T_{\mathrm{i}} + \frac{5}{2}nT_{\mathrm{i}}\mathbf{v}_{\parallel}\right)\\ &\quad +\nabla_{\perp}\cdot\left(-\chi_{\mathrm{i}}n\nabla_{\perp}T_{\mathrm{i}} - \frac{5}{2}T_{\mathrm{i}}D\nabla_{\perp}n\right)\\ &= k(T_{\mathrm{e}} - T_{\mathrm{i}}) + S_{\mathrm{ei}},\end{aligned} \tag{4}$$

where $p = n(T_{\mathrm{e}} + T_{\mathrm{i}})$ and $\eta_{\perp} = m_{\mathrm{i}}nD$. The variables p, n, m and T represent pressure, density, mass, and temperature, respectively. The subscripts i and e indicate ions and electrons, respectively. The subscripts $\perp$ and $\parallel$ indicate the perpendicular and parallel directions of the magnetic field, respectively. The parallel transport coefficients, $\eta_{\parallel}$, κ_{e} and κ_{i} are considered to be classical, while the cross-field transport coefficients, D, χ_{e} and χ_{i} are anomalous and usually determined according to experiments. Source terms, S_{p}, S_{m}, S_{ee} and S_{ei} are the particle, momentum and energy source arising from plasma-neutral interactions such as ionization, excitation and charge exchange. EMC3 is self-consistently coupled with EIRENE, which solves the kinetic Boltzmann equations for neutral particles. EMC3-EIRENE solves a steady-state distribution of plasma and neutral particles through iterative calculations, and each iteration uses values obtained from the previous iteration step.

2.2 Generation of the 3D grid system

The magnetic field of Heliotron J has $l/m = 1/4$ helical periodicity and the poloidal cross-sections at toroidal angles $\phi = 0°$ and 45° have up-down symmetry. Figure 1 shows contour plots of the connection length on the poloidal cross-sections. Quantities of the vacuum magnetic field are obtained using the KMAG [24,25] code. The simulation box size for the EMC3-EIRENE calculation is 45° in the toroidal direction, i.e., a half helical section, and the full-torus is modeled effectively using the helical periodicity and an assumption of up-down symmetry at $\phi = 0°$ and 45°.

As shown in Fig. 1 (b), there are seven "points" like the X-point of a tokamak divertor. A pair of divertor legs connected to the X-point on $(\phi, \theta) = (0, 0)$ is in contact with the chamber wall. The structure of the connection length in the SOL region is determined by the vacuum wall in Heliotron J, where the wall works like a limiter in tokamaks. As shown in the contour plot in Fig. 1 (b), magnetic field lines in the SOL are connected to a local region in both the poloidal/toroidal directions (see blue arrows shown in Fig. 1 (b)). In the other region, the connection length on the wall is quite small. Note that it seems that only a pair of divertor legs is connected to the wall, but all the magnetic field lines in the divertor legs are also connected to

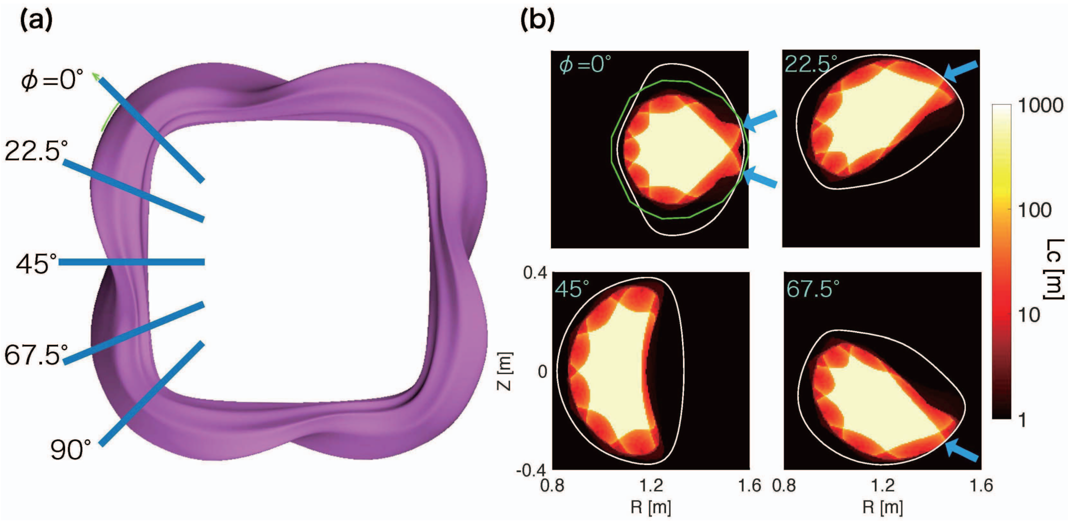

Fig. 1 (a) Top view of Heliotron J plasma. (b) Contour plots of connection length on poloidal cross-sections every 22.5°. The plot on $\phi = 90°$ is equal to $\phi = 0°$. The white line represents the chamber wall. The green line on poloidal cross-section $\phi = 0$ represents the outermost boundary for plasma modeling.

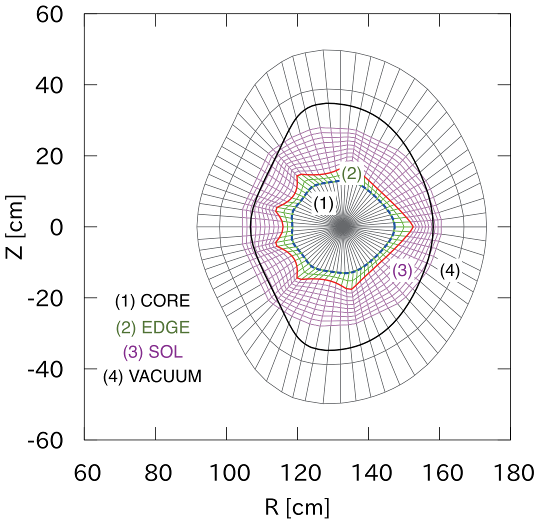

Fig. 2 The computational grid at $\phi = 0°$ generated based on the vacuum magnetic field for the standard configuration. The bold red line represents the LCFS, and the bold black line represents the vessel wall.

the chamber wall at the same poloidal/toroidal location indicated by the blue arrows in Fig. 1 (b).

The 3D grid of Heliotron J has been generated for the EMC3-EIRENE calculation; it has four domains: CORE, EDGE, SOL and VACUUM. These domains are shown in Fig. 2 and labeled (1) - (4), respectively. The confined region of the plasma is covered by the CORE and EDGE domains. The boundary between the CORE and EDGE domains is set at $r/a \simeq 0.8$ and the outer boundary of the EDGE domain is at the last closed flux surface (LCFS). The area outside of the LCFS is covered by the SOL and VACUUM domains. The outer boundary of the SOL domain is defined to cover the region with connection length $L_c > 10$m, see Fig. 1 (b). The VACUUM domain is defined to cover chamber wall. Neutral particle transport is solved in the entire domains and plasma transport is solved only in the EDGE and SOL domains. The grid points in these domains have field-aligned structures in the toroidal direction to reduce aliasing error arising from the finite resolution of the grids.

In the grid generation procedure, we combined the grid generator tool FLARE [26] and an additional code developed by ourselves. The 3D grid is generated by the following FLARE code procedures;

(a) generate a 2D base grid of the EDGE domain on the cross section at $\phi = 0°$;

(b) expand the outer boundary of the EDGE domain and generate a SOL domain of the base grid above;

(c) trace field lines in the toroidal direction from each node of the base grid and generate a 3D grid;

(d) generate the VACUUM and CORE domains.

In the procedure (b), the SOL grid between LCFS, i.e., the outer boundary of the EDGE domain, and the outer boundary of SOL domain was generated manually by our additional code. This is because FLARE code cannot complete the procedure (c), due to a problem when a field line goes to outside of the prepared magnetic field data when we cover whole peripheral plasma on the cross section in procedure (b). The separation of the plasma domains at the LCFS with our additional code realizes the flux-surface aligned grid in EDGE domain and the sufficiently large SOL domain simultaneously.

Table 1 Cell number of the grid system we prepared. The grid 1 is the coarsest and the grid 4 is the finest. The cell number in the toroidal direction is 90 in all grids.

	radial				poloidal
	CORE	EDGE	SOL	VAC	
grid 1	5	15	15	10	120
grid 2	5	15	45	10	120
grid 3	5	15	15	10	360
grid 4	5	15	45	10	360

We generated multiple grids of the standard configuration of Heliotron J with a variety of resolutions using the procedure above. In this article, as shown in Table 1, we show typical four examples with different cell numbers in the radial/poloidal resolutions to check the effect of grid resolution on calculation results. The toroidal resolution is common to all domains. A large cell number means a high resolution in the directions.

3. Results and Discussion

3.1 Typical calculation results

We carried out EMC3-EIRENE simulations with the following parameters; input heating power: $P = 200$ kW, electron density upstream (blue dashed line in Fig. 2) of the plasma grid: $n_e = 0.8 \times 10^{19}$ m^{-3}. The perpendicular transport coefficients are assumed as follows; $D = 0.5$ m^2/s and $\chi = 2$ m^2/s. Figure 3 shows the calculation results of electron density (Fig. 3 (a)), electron temperature (Fig. 3 (b)), Mach number (Fig. 3 (c)), and hydrogen atom density (Fig. 3 (d)). The distributions of electron density and temperature reflect the structure of the connection length shown in Fig. 1. The Mach number distribution suggests a poloidal modulation of plasma flow along the divertor legs. The hydrogen atom density is locally high because of recycling by the divertor legs.

3.2 Convergence of calculation

The EMC3-EIRENE code solves the equations iteratively. The number of MC particles is increased step by step to save calculation time. Figure 4 (a) shows the number of Monte Carlo particles during the iterative calculations in the EMC3-EIRENE operation. In this figure, we compared two methods to increase the number of MC particles up to 2 million. As shown in Fig. 4 (b), the divertor

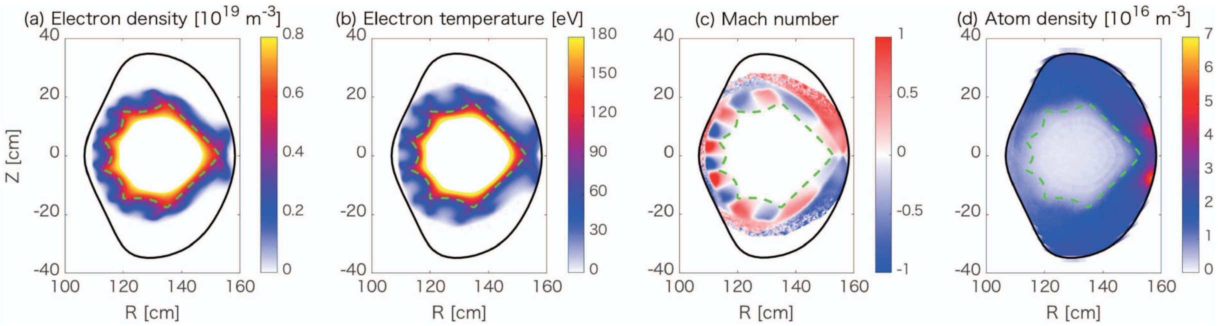

Fig. 3 Contour plot of (a) electron density, (b) electron temperature, (c) Mach number, and (d) hydrogen atom density on the plane $\phi = 0°$ with the standard magnetic configuration. The dashed green line represents the LCFS, and the bold black line represents the vessel wall.

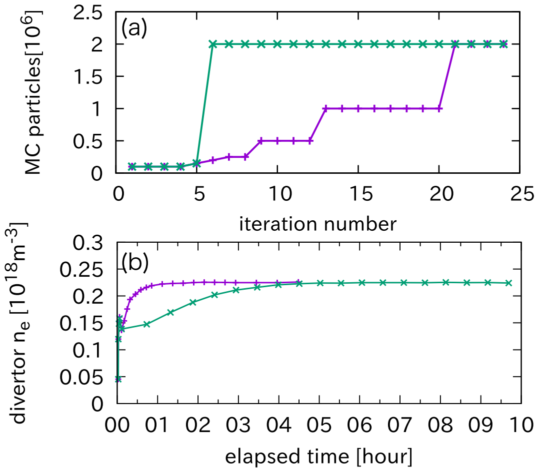

Fig. 4 (a) Number of Monte Carlo (MC) particles during iterative calculations. (b) Convergence of electron density during calculations. The same color of plots represents the same calculation between (a) and (b).

electron density converged within 1 to 2 hours when the number of MC particles was increased step by step. On the other hand, when the number of MC particles is increased with one step, the convergence of electron density takes 4 or 5 hr. We use the acceleration method with MC particles increased step by step in the calculations given below.

We checked the convergence of the calculation results at each calculation step. To check the status of convergence, we plotted (a) relative change of n_{e}, (b) relative change of T_{e}, (c) downstream n_{e}, and (d) downstream T_{e} at different radial and poloidal resolutions in Fig. 5. Here n_{e}^{ds} and T_{e}^{ds} are the pressure-weighted average for the downstream cells just in front of the plasma-facing walls, and have the following form:

$$n_{\mathrm{e}}^{ds} = \frac{\sum_{l=1}^{np} P^{(l)} V^{(l)} n_{\mathrm{e}}^{(l)}}{\sum_{l=1}^{np} P^{(l)} V^{(l)}}, \tag{5}$$

$$T_{\mathrm{e}}^{ds} = \frac{\sum_{l=1}^{np} P^{(l)} V^{(l)} T_{\mathrm{e}}^{(l)}}{\sum_{l=1}^{np} P^{(l)} V^{(l)}}. \tag{6}$$

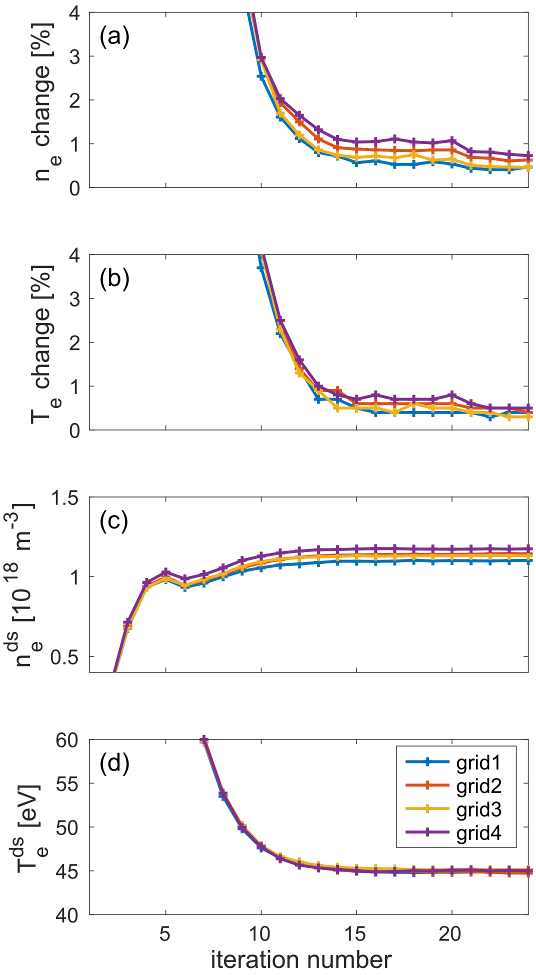

Fig. 5 Effect of radial resolution in the SOL domain during iterative calculations about (a) relative change of electron density, (b) relative change of electron temperature, (c) downstream electron density and (d) downstream electron temperature.

The variable P is local plasma pressure, of the form

$$P = n_{\mathrm{e}}(T_{\mathrm{e}} + T_{\mathrm{i}}), \tag{7}$$

V is a volume of a cell. The summation $\sum_{l=1}^{np}$ is taken over downstream cells, where “downstream” is basically

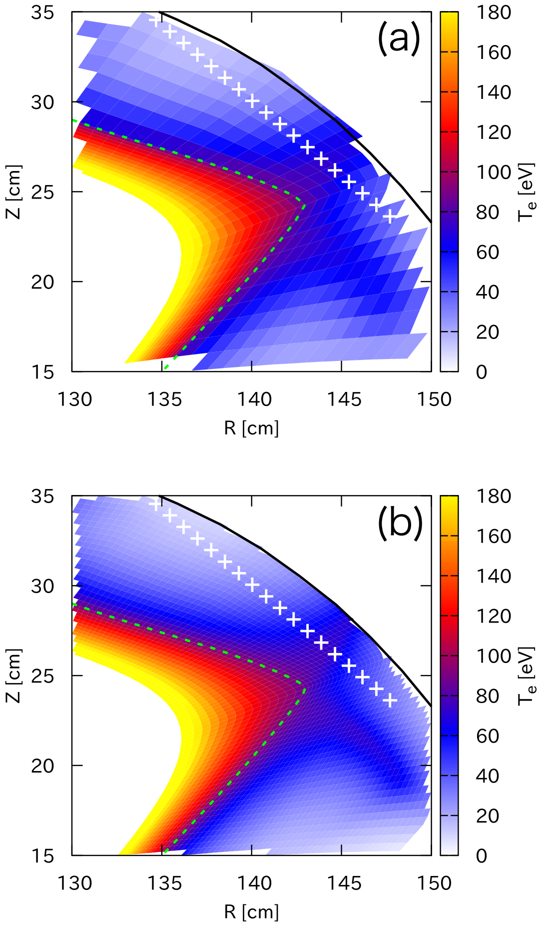

Fig. 6 Electron temperature of the ϕ = 22° plane calculated with (a) grid 1, (b) grid 4. The green dashed line indicates the LCFS.

defined as the outermost cells of the SOL domain grids, where SOL plasma exists. The variable np indicates the cell number in the poloidal direction. Relative change is the change ratio compared with previous iterative calculation results.

The relative error apparently decreases with the increase in MC particles in Figs. 5 (a) and (b). Statistical error increases slightly with the grid resolution, because there are fewer MC particles per cell with larger resolutions. Even in the finest resolution case, i.e., grid 4 in Table 1, the relative errors of n_e and T_e maintain values below 1% after convergence. Similarly, n_e^{ds} and T_e^{ds} also converge to certain values during iterative calculations in Figs. 5 (c) and (d). These results show that influence of grid resolution upon the calculation result is small enough practically, for example, compared to the accuracy of experimental measurements. However, the downstream electron density tends to increase with a finer grid, and it is necessary to choose a sufficient resolution carefully to solve particle transport correctly.

3.3 Comparison with the experimental setup

All calculation results with resolutions shown in Sec. 3.2 converge to certain values properly, and the grid resolution should satisfy the spatial resolution required for the comparison with experimental measurements.

For example, the electron temperatures of divertor legs with different resolutions are compared in Figs. 6 (a) and (b), which show the electron temperature in a part of the ϕ = 22° plane with grids 1 and 4, respectively. It can be seen that a much smoother spatial distribution structure is obtained in Fig. 6 (b) compared to that in Fig. 6 (a). White cross-markers shown in Fig. 6 are the measurement points of the divertor probe array of Heliotron J [23].

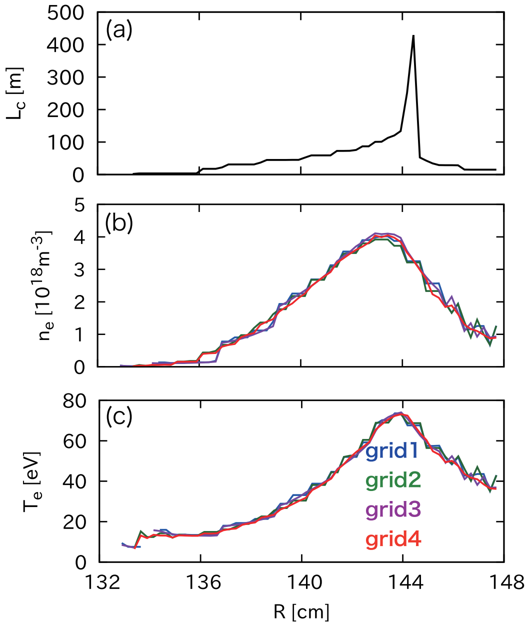

Fig. 7 (a) connection length, (b) electron density, and (c) electron temperature along the line connecting the white markers in Fig. 6.

The distributions of connection length, electron density and electron temperature along the white markers in Fig. 6 are shown in Fig. 7. The structures of the electron density and temperature are roughly captured even with the lower resolution grids, without changing the peak value or spatial gradient. However, smoother and more natural distributions can be seen with the higher resolution grids.

4. Summary

The EMC3-EIRENE code has been successfully applied to Heliotron J. A 3D grid with a field-aligned structure is required for the EMC3-EIRENE calculation. A grid generation tool, FLARE, is utilized to create the grid in conjunction with the additional code we developed. We generated multiple grids with different radial and poloidal resolutions. Calculations converged with all grids, regardless of resolution. The relative change of electron density and temperature compared with the previous iterative calculation is reduced less than 1%. The detailed structure of the peripheral plasma is obtained by the fine grid. Electron density is slightly changed by changing grid resolution, and we should explicate the cause of this through further research. However, the effect of grid resolution is small enough to practically compare with the experimental measurements. Comparison with measurements should be taken into consideration when discussing the grid resolution.

Acknowledgments

The authors are grateful to the Heliotron J staffs for useful discussion. This work was supported partly by JSPS KAKENHI Grant Number 16K18340. This work was performed with the support and under the auspices of the NIFS Collaborative Research Program (NIFS10KUHL030, NIFS17KUHL081, NIFS 18KUHL084, NIFS18KNTT047), the Collaboration Program of the Laboratory for Complex Energy Processes, Institute of Advanced Energy, Kyoto University, Future Energy Research Association and JSPS Core-to-Core Program, A. Advanced Research Networks.

[1] P.C. Stangeby and G.M. McCracken, Nucl. Fusion **30**, 1225 (1990).
[2] A.S. Kukushkin *et al.*, Nucl. Fusion **49**, 075008 (2009).
[3] Y. Feng *et al.*, Nucl. Fusion **49**, 095002 (2009).
[4] A. Loarte *et al.*, Nucl. Fusion **47**, 203 (2007).
[5] S. Masuzaki *et al.*, Nucl. Fusion **42**, 750 (2002).
[6] T.E. Evans *et al.*, Nature Physics **2**, 419 (2006).
[7] M. Kobayashi *et al.*, Nucl. Fusion **55**, 104021 (2015).
[8] Y. Feng *et al.*, Contrib. Plasma Phys. **44**, 57 (2004).
[9] D. Reiter *et al.*, Fusion Sci. Technol. **47**, 172 (2005).
[10] Y. Feng *et al.*, Nucl. Fusion **56**, 126011 (2016).
[11] F. Effenberg *et al.*, Nucl. Fusion **57**, 036021 (2017).
[12] H. Frerichs *et al.*, Nucl. Fusion **57**, 126022 (2017).
[13] M. Kobayashi *et al.*, Fusion Sci. Technol. **58**, 220 (2010).
[14] G. Kawamura *et al.*, Contrib. Plasma Phys. **54**, 437 (2014).
[15] G. Kawamura *et al.*, Plasma Phys. Control. Fusion **60**, 084005 (2018).
[16] S. Dai *et al.*, Plasma Phys. Control. Fusion **59**, 085013 (2017).
[17] S. Dai *et al.*, Nucl. Fusion **58**, 096024 (2018).
[18] T. Lunt *et al.*, Nucl. Fusion **52**, 054013 (2012).
[19] J. Huang *et al.*, Plasma Phys. Control. Fusion **56**, 075023 (2014).
[20] T. Obiki *et al.*, Nucl. Fusion **41**, 833 (2001).
[21] T. Mizuuchi *et al.*, Fusion Sci. Technol. **50**, 352 (2006).
[22] T. Mizuuchi *et al.*, J. Nucl. Mater. **363-365**, 600 (2007).
[23] T. Mizuuchi *et al.*, J. Nucl. Mater. **313-316**, 947 (2003).
[24] Y. Nakamura, J. Plasma Fusion Res. **69**, 41 (1993).
[25] M. Wakatani *et al.*, Nucl. Fusion **40**, 569 (2000).
[26] H. Frerichs *et al.*, Comput. Phys. Commun. **181**, 61 (2010).